


## Correspondence between flow structures and heat transfer in regime transitions in turbulent rotating thermal convection

Lin Sun 

*Center for Complex Flows and Soft Matter Research, [Southern University of Science and Technology](#),  
Shenzhen 518055, China;*


*Department of Mechanics and Aerospace Engineering, [Southern University of Science and Technology](#),  
Shenzhen 518055, China;*

*and Department of Mechanical Engineering, The [University of Hong Kong](#), Hong Kong, China*


Yun-Bing Hu \*

*Center for Complex Flows and Soft Matter Research, [Southern University of Science and Technology](#),  
Shenzhen 518055, China*

*and Department of Mechanics and Aerospace Engineering, [Southern University of Science and Technology](#),  
Shenzhen 518055, China*

Li-Qiu Wang 

*Department of Mechanical Engineering, The [Hong Kong Polytechnic University](#), Hong Kong, China*

Ke-Qing Xia †

*Center for Complex Flows and Soft Matter Research, [Southern University of Science and Technology](#),  
Shenzhen 518055, China;*

*Department of Mechanics and Aerospace Engineering, [Southern University of Science and Technology](#),  
Shenzhen 518055, China;*

*and Department of Physics, [Southern University of Science and Technology](#), Shenzhen 518055, China*



(Received 13 June 2024; accepted 3 December 2024; published 23 December 2024)

We present an experimental study of the properties of heat transport and flow structures in rotating thermal convection. The heat-transfer efficiency is found to exhibit a scaling transition at a transitional Ekman number  $Ek_t$ , at which sharp transitions of the dynamical and geometrical properties of the columnar structures also occur. This precise correspondence implies that the behaviors of heat-transfer efficiency are intimately related to the changes in the coherent structures in the bulk flow. The sharp transition at  $Ek_t$  provides the first unambiguous experimental evidence for the regime transition from convective Taylor column regime to plume regime, at which the columns break down due to the increased inertial effect. Compared to the heat-transport behaviors, the transitions of the flow-field statistics are much sharper, which suggests that in further investigations of regime transitions, flow-field measurements may be used to provide a more definitive criterion.

DOI: [10.1103/PhysRevFluids.9.123501](https://doi.org/10.1103/PhysRevFluids.9.123501)

---

\*Contact author: [huyunbing1991@gmail.com](mailto:huyunbing1991@gmail.com)

†Contact author: [xiakq@sustech.edu.cn](mailto:xiakq@sustech.edu.cn)

## I. INTRODUCTION

Many fascinating natural phenomena, such as the polar vortices [1,2] and starspots [3], are closely related to the coherent structures existing in the geophysical and astrophysical systems. These structures are believed to play an important role in the systems' mass, momentum, and energy transfer [4]. Understanding their underlying connections is a crucial issue when inferring the celestial bodies' inner structures. Rotating Rayleigh-Bénard convection (RRBC), which describes a rotating fluid layer sandwiched between a hot bottom plate and a cold top plate [5–7], is a widely studied local planar model that can be used to understand these spherical systems [8]. RRBC is characterized by multiple control parameters. The Rayleigh number  $Ra = \alpha g \Delta T H^3 / (\nu \kappa)$  describes the strength of the buoyancy force. The significance of the Coriolis force can be assessed using the Ekman number  $Ek = \nu / (2\Omega H^2)$ . The remaining control parameters are the Prandtl number  $Pr = \nu / \kappa$  and the diameter-to-height aspect ratio  $\Gamma = 2R/H$ . Here,  $\alpha$ ,  $\nu$ , and  $\kappa$  represent the thermal expansion coefficient, kinematic viscosity, and thermal diffusivity of the working fluid, respectively.  $\Delta T$  corresponds to the temperature difference across the fluid layer, and  $\Omega$  denotes the rotation speed antiparallel to the gravity  $g$ .

In RRBC, the Coriolis force exerts a vertical "stiffness" on the flow to form two-dimensional columns, whereas the buoyancy force tends to generate three-dimensional flow structures [9]. The competition of these two forces results in various coherent structures in different regimes [10,11]. Due to the increased inertial effects at larger  $Ra$  [12], the convective Taylor columns (CTC) in the CTC regime first break down into plumes in the plume regime, and then become fragmented in the geostrophic turbulence regime. At large enough  $Ra$ , the RRBC system conforms to the nonrotating one. The different heat-transport behaviors (quantified by the Nusselt number  $Nu$ ) [13] are believed to be related to these various structures. For example, the CTCs, connecting the lower and upper thermal boundary layers directly, act as an efficient pathway for heat transport, resulting in a steep  $Nu - Ra$  scaling.

However, it is difficult to establish an exact correspondence between heat transfer and flow structures in RRBC. For example, due to its gradual behaviors in crossing different flow regimes [14], Cheng *et al.* [15] have shown that heat-transfer measurement alone is not sufficient to determine regime transitions; instead, mid-height temperature gradients exhibit consistent transitions with those of simulated flow structures. In RRBC, even for the most obvious transition from CTC regime to plume regime (at which CTCs break down and steep  $Nu - Ra$  scaling ends), different transitional values exist [6,14]. Analyses of flow fields obtained from asymptotic simulations suggest that this transition occurs at  $RaEk^{4/3} = 55$  [16], which is roughly verified by PIV measurements [17,18]. Nevertheless, another prediction  $RaEk^{1.47} = 5.4$  was provided for this transition by extrapolating the steep  $Nu - Ra$  scaling to meet the nonrotation scaling [19]. If this criterion is determined by intersecting two locally fitted power laws, the result becomes  $RaEk^{1.6} = 1.18$  (depends on  $\Gamma$ ) [20]. Although these criteria have some consistency by considering the fact that they are obtained from different quantities under different control parameter ranges [6], a definite correspondence between heat transfer and flow structures is still lacking in RRBC. The solution to this issue needs simultaneous measurements of heat transfer and flow structures.

In this paper, heat transport and flow structures are investigated experimentally. Our experiments reveal that both heat transfer efficiency and the dynamical and geometrical properties of the columnar structures exhibit a transition at the same transitional Ekman number  $Ek_t$ . This precise correspondence not only suggests that the heat transfer is intimately dependent on the properties of coherent structures in the rapidly rotating regime, but also provides, to the best of our knowledge, the first unambiguous experimental evidence on when the columns break down in RRBC.

The remainder of this paper is organized as follows. In Sec. II, the experimental setup and the parameters are introduced. Section III presents the main experimental results, including the global heat-transport properties, flow dynamics, and geometrical properties of columnar structures. Finally, conclusions and implications of the study are provided in Sec. IV.

## II. EXPERIMENTAL SETUP AND THE PARAMETERS

### A. The experimental setup

All the rotating experiments, encompassing heat transport and flow-field measurements, were performed on a home-built rotating table. The design of the rotating table has been described in detail in Ref. [21], and we will not delve into its specifics here. The convection cell for heat-transport measurements was an upright cylinder with a height  $H = 96.15$  mm and a diameter  $2R = 191.95$  mm, resulting in an aspect ratio of  $\Gamma = 2R/H = 2$ . The heat flux  $q$  was applied to the hot plate by heating nichrome wires and was then extracted by the cold plate, which was cooled by a temperature-controlled water bath. The temperatures of the hot ( $T_h$ ) and cold ( $T_c$ ) plates were measured using four thermistors in each plate. Water was used as the working fluid and its properties, i.e., the thermal expansion coefficient  $\alpha$ , the kinematic viscosity  $\nu$ , the thermal diffusivity  $\kappa$ , and the thermal conductivity  $\lambda$ , were calculated at  $T_0 = (T_h + T_c)/2 = 40.0^\circ\text{C}$  and the corresponding Prandtl number  $\text{Pr} = \nu/\kappa$  was 4.34. To ensure a precise measurement of the heat-transport efficiency (i.e., the Nusselt number  $\text{Nu} = qH/\lambda\Delta T$ ), a copper basin was placed beneath the bottom plate to prevent heat leakage, and the whole convection cell was wrapped by several layers of Styrofoam and then placed in a thermostat to minimize the influence of the surrounding environment [Fig. 1(a)]. During each experiment, the desired Rayleigh number  $\text{Ra}$  for the system without rotation was first set by adjusting the temperatures of the top and bottom plates. Then, the rotating table was accelerated to the specified speed very slowly (around 6 rpm/min). Due to rotation effects, the temperatures of the top and bottom plates changed. Therefore, they must be adjusted back to the original values very carefully so that the desired  $\text{Ra}$  was reached again. After the system reached a stable state, the data were further collected for more than four hours.

The flow fields were visualized using the particle image velocimetry (PIV) technique, where some modifications had to be made to the convection cell. The hot plate was coated with black nickel to minimize the influence of reflected laser on the images. Additionally, a rectangular jacket, filled with degassed and deionized water, was fitted outside the cylindrical sidewall to prevent optical distortion. Since the transitions between different flow states of the RRBC system are ambiguous, we have to first measure the vertical flow fields to identify the cases with columnar structures. These flow fields, passing through the centerline of the cell, were illuminated by a continuous 532 nm laser and recorded for 20 min by an iDS camera with a resolution of  $2048 \times 1024$  pixels and a frequency of  $\sim 10$  Hz [Fig. 1(b)]. A typical example for  $\text{Ra} = 1.63 \times 10^8$  is presented in Fig. 2. It can be seen that as  $\text{Ek}$  increases, the well-defined columns shown in Fig. 2(a) first break down [Figs. 2(b) and 2(c)]. However, the columnar structures in these cases still penetrate deeply into the bulk region. If  $\text{Ek}$  increases further, the coherent structures become too fragmented to be regarded as columnar structures here [Fig. 2(d)]. Thus, their geometrical properties will not be investigated in the present work.

Once the cases with columnar structures were identified by eye, the properties of these structures were further investigated by measuring the horizontal fields at height  $z = H/4$  [Fig. 1(c)]. In these experiments, the top plate was replaced with a sapphire disk, and a high-performance CMOS camera (FLIR. ORX-10G) with a resolution of  $3000 \times 3000$  pixels was mounted above the cell. The flow fields were recorded for one hour at a frequency of  $2 \sim 20$  Hz, depending on the  $\text{Ra}/\text{Ra}_c$  values. Here,  $\text{Ra}_c = 8.7\text{Ek}^{-4/3}$  is the onset Rayleigh number for convection to set in Ref. [22]. All the recorded raw images were processed using a commercial PIV system (Lavison). Velocity vectors were calculated using a  $32 \times 32$  pixel interrogation window, with a 50% overlap between neighboring subwindows.

### B. The parameter space

All the rotating experiments were performed at fixed aspect ratio  $\Gamma = 2$  and Prandtl number  $\text{Pr} = 4.34$ . The Rayleigh number  $\text{Ra}$  ( $3.50 \times 10^7 \leq \text{Ra} \leq 7.56 \times 10^8$ ) and the Ekman number

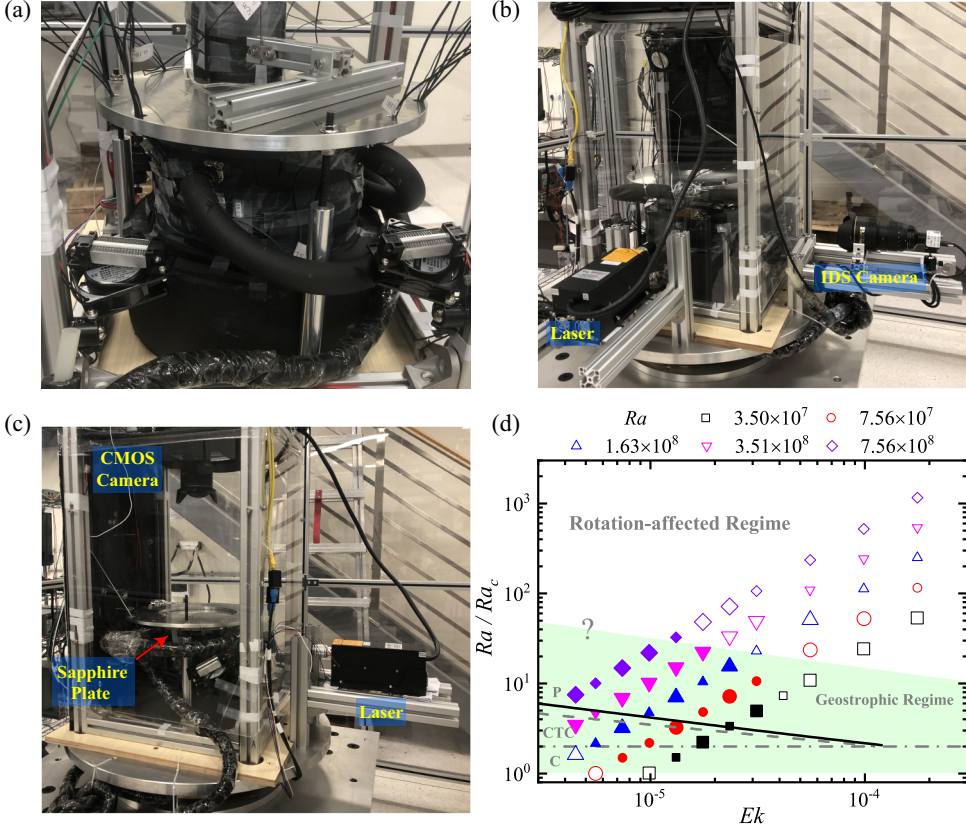


FIG. 1. Panels (a)–(c) are the experimental setups for heat-transport measurements, and vertical and horizontal flow-field measurements, respectively. In panel (b), the vertical plane passing through the centerline of the convection cell is illuminated by a laser sheet, and the corresponding flow fields are recorded by an iDS camera. In panel (c), the horizontal flow field at height  $z = H/4$  is illuminated by the horizontal laser sheet and recorded by a camera placed above the cell. (d) The space of  $Ra/Ra_c - Ek$  covered by the present study. The solid symbols and the symbols with larger size are the cases in which the horizontal ( $z = H/4$ ) and the vertical flow fields are measured by PIV, respectively. This space is divided into a rotation-affected regime and a geostrophic regime (roughly indicated by the shaded area since the transition between them is not clear [6]). The geostrophic regime can be further divided into several subregimes, i.e., the cells (C), the convective Taylor columns (CTC), and the plumes (P) regimes, which are separated by  $Ra/Ra_c = 2$  [11] (dot-dashed line) and  $Ra_{r1} = 1.18Ek^{-1.6}$  [20] (gray dashed line), respectively. The black solid line  $RaEk^{1.66} = 0.71$  is obtained from the present study.

$Ek$  ( $4.49 \times 10^{-6} \leq Ek \leq 1.76 \times 10^{-4}$ ) were changed by varying the temperature difference  $\Delta T$  ( $1.0 \leq \Delta T \leq 22.6$  K) and the rotation speed  $\Omega$  ( $1.9 \leq \Omega \leq 76.0$  rpm), respectively. The detailed parameters covered by the present study are shown in the  $Ra/Ra_c - Ek$  space in Fig. 1(d).

According to Ref. [6], this parameter space can be divided into two regimes, i.e., the rotation-affected regime and the geostrophic regime, and the separation between them is difficult to determine precisely. The geostrophic regime, which is dominated by the Coriolis force, can be further divided into several subregimes, namely, the cellular regime (C), the convective Taylor column regime (CTC), and the plume regime (P). The cellular regime and the CTC regime are separated by the gray dot-dashed line  $Ra/Ra_c = 2$  [11], whereas the transition from the CTC regime to the plume regime occurs at  $Ra_{r1} = 1.18Ek^{-1.6}$  [20] (gray dashed line), which is close to the black solid line  $RaEk^{1.66} = 0.71$  obtained from the present study.

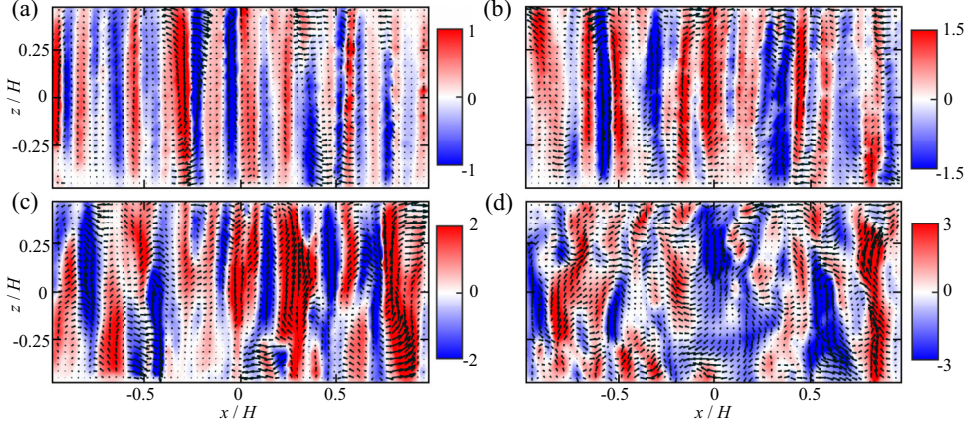


FIG. 2. The vertical flow fields for  $Ra = 1.63 \times 10^8$  and (a)  $Ek = 7.41 \times 10^{-6}$  ( $Ra/Ra_c = 3.2$ ), (b)  $Ek = 1.32 \times 10^{-5}$  ( $Ra/Ra_c = 7.1$ ), (c)  $Ek = 2.34 \times 10^{-5}$  ( $Ra/Ra_c = 15.5$ ), and (d)  $Ek = 5.56 \times 10^{-5}$  ( $Ra/Ra_c = 51.1$ ). These cases are indicated by the solid symbols in Fig. 3. These fields are averaged over one second. The color bars are coded with the magnitude of the vertical velocity  $w$  in units of mm/s.

In Fig. 1(d), all the symbols represent the cases where heat-transport measurements were conducted. Among these symbols, the ones with larger size are the cases where the vertical flow fields were measured using PIV, and the solid symbols are the cases where the horizontal flow fields were measured. More specifically, both the vertical and horizontal flow fields were measured for larger solid symbols, whereas only the horizontal (vertical) flow fields were measured for the small solid symbols (larger open symbols).

The centrifugal effect is quantified by the Froude number  $Fr = \Omega^2 R/g$ . Its range in the present study is  $4 \times 10^{-4} \leq Fr \leq 6.2 \times 10^{-1}$ , which has reached the weak-centrifugal regime with  $Fr_c < Fr < \Gamma/2$  ( $Fr_c = 3.79 \times 10^{-7} Ra^{0.53}$ ), but well below the strong-centrifugal regime with  $Fr > \Gamma/2$  [21,23]. In Appendix B, we show that the properties of columnar structures are not affected by the weak centrifugal force.

### III. RESULTS AND DISCUSSIONS

#### A. The global heat transport and the regime transition

The heat transport properties are first examined. Figure 3(a) shows the Nusselt number  $Nu$  as a function of  $Ra/Ra_c$ , which exhibits a steep scaling  $Nu = 2.5(Ra/Ra_c)^\gamma$  (with  $\gamma = 1.5 \pm 0.3$ ) before transitioning to a saturated state. It can be seen from Appendix A that these results agree excellently well with the theoretical model proposed recently [7], suggesting a good quality of our measured data.

With the measured nonrotating result  $Nu_0 = 0.144Ra^{\gamma_0}$  with  $\gamma_0 = 0.292 \pm 0.001$  (refer to Appendix A), one may rescale the steep scaling as  $Nu/Nu_0 \sim (RaEk^\beta)^{\gamma-\gamma_0}$  [20], with  $\beta \equiv 4\gamma/3(\gamma - \gamma_0) = 1.66 \pm 0.08$ . Therefore, in Fig. 3(b), the reduced Nusselt number  $Nu/Nu_0$  is plotted as a function of  $RaEk^{1.66}$  and the data for different  $Ra$  collapse on top of each other, which suggests that the steep-scaling regime has a unified upper bound that can be obtained by two different ways. Lu *et al.* [20] determined this value by intersecting two locally fitted power laws [see the example shown in the inset of Fig. 3(b)]. In our measurements, the corresponding results are indicated by the colored vertical dashed lines in Fig. 3(b), which give out a mean value of  $RaEk^{1.66} = 0.71 \pm 0.04$ . The other method is to extrapolate the steep  $Nu - Ra$  scaling to meet the nonrotating results [19], as indicated by the vertical cyan dashed line with  $RaEk^{1.66} = 0.914$ . It can be shown that the result obtained by the latter method overestimates the upper bound a bit [24]. Therefore, in the present

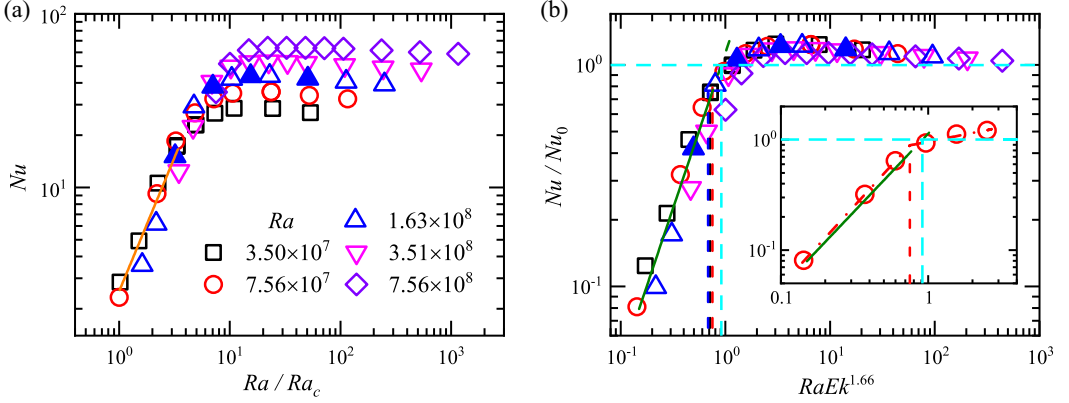


FIG. 3. (a) The Nusselt number  $Nu$  is plotted as a function of  $Ra/Ra_c$ . The orange solid line is the power-law fitting  $Nu = 2.5(Ra/Ra_c)^{1.5 \pm 0.3}$ . (b) The reduced Nusselt number  $Nu/Nu_0$  is plotted as a function of  $RaEk^{1.66}$ , where  $Nu_0$  is the nonrotating value. The rapidly increasing data are described by a steep scaling  $Nu/Nu_0 = 1.13(RaEk^{1.66})^{1.4 \pm 0.2}$  (the dark green solid line), which is extrapolated (the dark green dashed line) to intersect with  $Nu/Nu_0 = 1$  at  $RaEk^{1.66} = 0.914$  (the vertical cyan dashed line). The colored vertical dashed lines, with the respective values of  $RaEk^{1.66} = 0.68$  (blue),  $0.71$  (black), and  $0.75$  (red), are determined by intersecting two locally fitted power laws, as exemplified in the inset plot. The solid symbols in (a) and (b) represent the cases corresponding to the vertical flow fields shown in Fig. 2.

study,  $RaEk^{1.66} = 0.71$  is regarded as the upper bound of the steep-scaling regime, from which a transitional Ekman number  $Ek_t$  can be derived, i.e.,

$$Ek_t = 0.81Ra^{-0.60 \pm 0.03}. \quad (1)$$

The scaling transition shown in Figs. 3(a) and 3(b) has been argued to be related to the changes of coherent structures in the bulk flow, i.e., the breakdown of CTCs into plumes at  $Ek_t$  (e.g., Refs. [11, 19]). To gain deeper insight into this transition, we will examine in detail both the dynamics and structures of the flow fields below.

### B. The properties of flow dynamics

Figure 2 displays some typical examples of vertical flow fields for  $Ra = 1.63 \times 10^8$  and four different values of  $Ek$ . By comparing with the  $Nu$  results in Fig. 3 (as indicated by the four solid triangles), it is evident that the well-defined and vertically uniform columns in the steep-scaling regime [Fig. 2(a)] gradually lose their coherence to form thermal plumes when  $Ek > Ek_t$  [Figs. 2(b) and 2(c)]. These qualitative visualizations suggest that the heat-transfer efficiency should be affected by the coherent structures in the bulk flow.

Figure 4 exhibits more quantitative results of the vertical flow fields in terms of their dynamic properties, namely, the mean absolute velocities that are calculated from the central region of these fields ( $|x/R| < 0.9$  and  $|z/(0.5H)| < 0.8$ ) to exclude the possible boundary effects. To reveal the underlying relation with the heat-transfer efficiency clearly, these spatially and temporally averaged absolute velocities (normalized by the free-fall velocity  $u_{ff} = \sqrt{\alpha g \Delta T H}$ ) are plotted as a function of  $\tilde{Ek} \equiv Ek/Ek_t$  in Fig. 4, where  $Ek_t$  is the transitional Ekman number at which the steep heat-transfer scaling ends [Eq. (1)].

Figure 4(a) shows the results of the absolute vertical velocity  $w_0 = \langle |w| \rangle$  ( $\langle \cdot \rangle$  denotes averaging over space and time), which exhibit a clear transition at  $\tilde{Ek} \approx 1$ . It can be seen that a rapid increase for  $\tilde{Ek} \lesssim 1$  is followed by a slower increment for  $\tilde{Ek} \gtrsim 1$ , with some variations for different  $Ra$ . As a comparison, the combined DNS (stars) and experimental (pluses) results from Ref. [25] are also displayed in Fig. 4(a). These results are obtained by varying  $Ra$  from  $2.2 \times 10^8$  to  $2.3 \times 10^{10}$

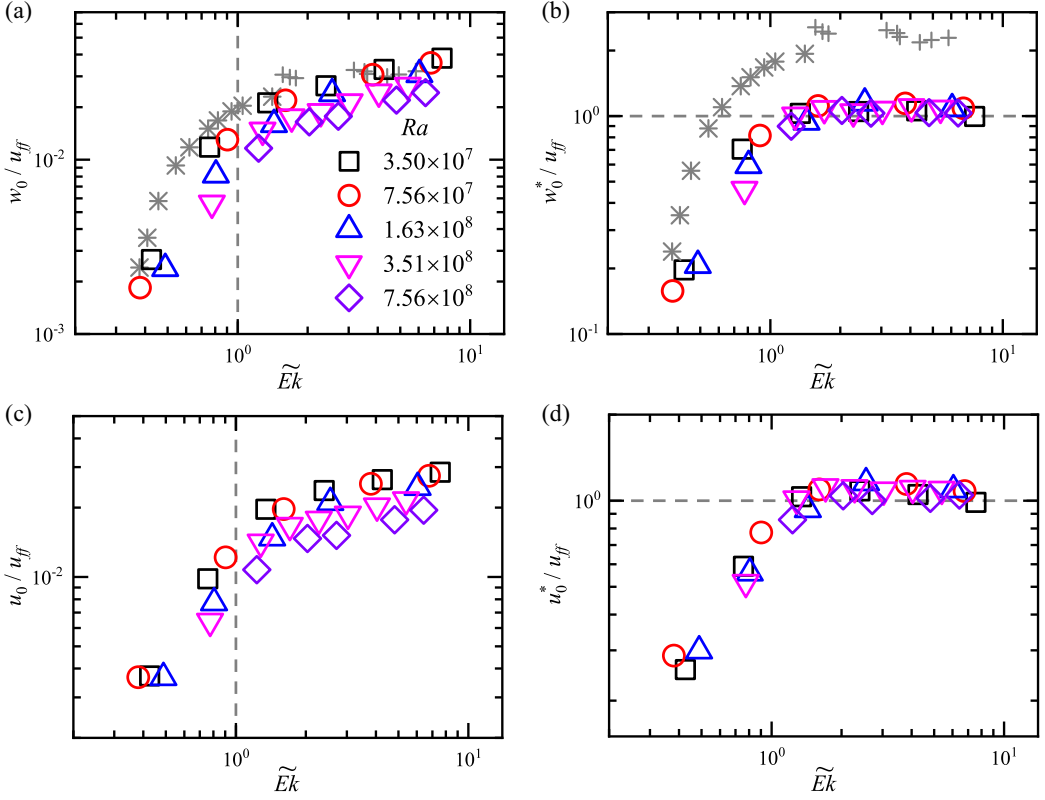


FIG. 4. (a) The mean absolute vertical velocity  $w_0 = \langle |w| \rangle$ , normalized by the free-fall velocity  $u_{ff}$ , is plotted as a function of  $\tilde{Ek} \equiv Ek/Ek_t$ , where  $Ek_t$  is the transitional Ekman number obtained from heat-transfer measurements. The data with gray symbols (star: DNS; plus: experiment) are from Ref. [25] with  $Ek = 3 \times 10^{-6}$  and various  $Ra$ . (b) The same data as in panel (a) but compensated by the scaling in the  $\tilde{Ek} \gtrsim 1$  regime, i.e.,  $w_0^* \equiv w_0 / [0.21 Ra^{-0.14} \tilde{Ek}^{0.36}]$ . Similar plots for the absolute horizontal velocity  $u_0 = \langle |u| \rangle$  are shown in panels (c) and (d), with  $u_0^* \equiv u_0 / [0.17 Ra^{-0.13} \tilde{Ek}^{0.24}]$ .

at fixed  $Ek = 3 \times 10^{-6}$ . Note that the experimental velocities from Ref. [25] are measured at a specific position in the flow fields, rather than spatial averaged as in the present case. Despite these differences, once these data are replotted as a function of  $\tilde{Ek}$ , a reasonable consistency with present results can be observed, i.e., both show a transition at  $\tilde{Ek} \approx 1$ . A direct two-dimensional fitting to the present data in each regime yields

$$\frac{w_0}{u_{ff}} = \begin{cases} 10.56 Ra^{-0.36 \pm 0.02} \tilde{Ek}^{2.3 \pm 0.1}, & \tilde{Ek} \lesssim 1; \\ 0.21 Ra^{-0.14 \pm 0.01} \tilde{Ek}^{0.36 \pm 0.02}, & \tilde{Ek} \gtrsim 1. \end{cases} \quad (2)$$

When  $w_0$  is compensated by the scaling in the  $\tilde{Ek} \gtrsim 1$  regime, i.e.,  $w_0^* \equiv w_0 / [0.21 Ra^{-0.14} \tilde{Ek}^{0.36}]$ , the transitions at  $\tilde{Ek} \approx 1$  become much clearer [Fig. 4(b)].

The same transition also occurs for the absolute horizontal velocity  $u_0 = \langle |u| \rangle$ , as can be observed in Figs. 4(c) and 4(d). The corresponding scalings for  $u_0$  are

$$\frac{u_0}{u_{ff}} = \begin{cases} 0.85 Ra^{-0.23 \pm 0.03} \tilde{Ek}^{1.6 \pm 0.1}, & \tilde{Ek} \lesssim 1; \\ 0.17 Ra^{-0.13 \pm 0.01} \tilde{Ek}^{0.24 \pm 0.02}, & \tilde{Ek} \gtrsim 1. \end{cases} \quad (3)$$

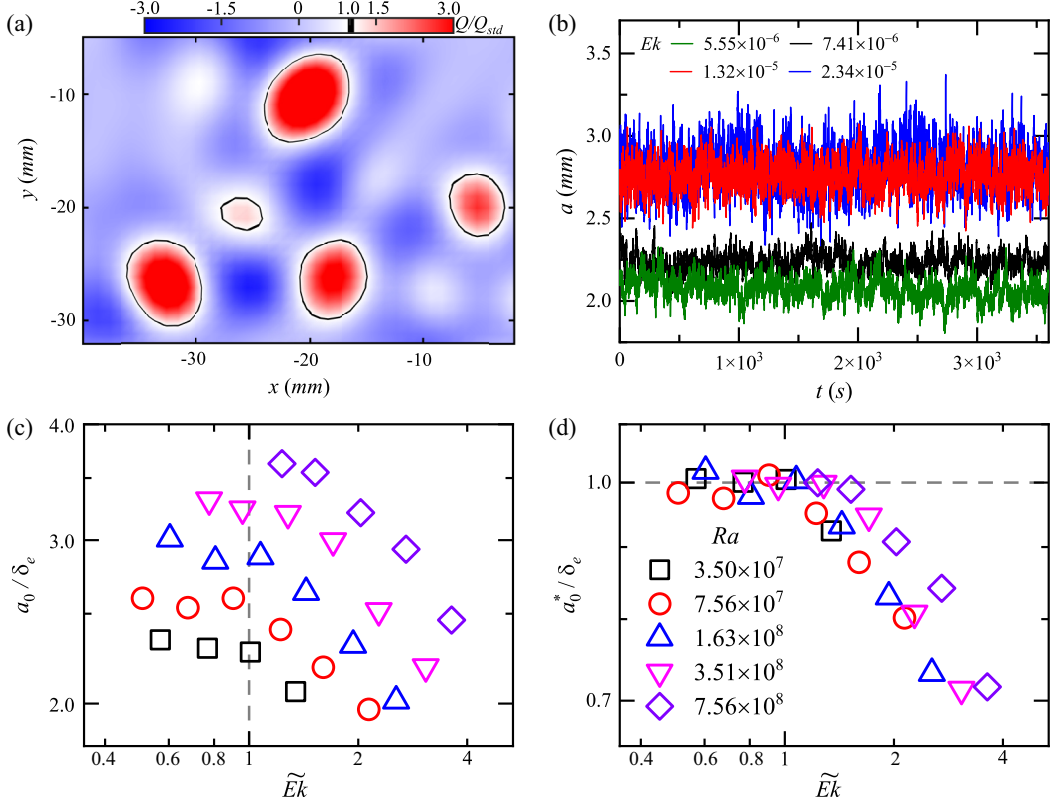


FIG. 5. (a) An instantaneous  $Q$  field for  $Ra = 3.50 \times 10^7$  and  $Ek = 1.76 \times 10^{-5}$  ( $Ra/Ra_c = 2.24$ ). The columns that are identified with the threshold value  $Q_{th} = Q_{std}$  are indicated by the black solid lines. (b) Time traces of the column's radius  $a(t)$  for  $Ra = 1.63 \times 10^8$  and different  $Ek$ . (c) The normalized mean radius  $a_0/\delta_e$  of columnar structures is plotted as a function of  $\tilde{Ek}$  for different  $Ra$ . Here,  $\delta_e = 3HEk^{1/2}$  [27] is the Ekman boundary-layer thickness. (d) The same data as in panel (a), but compensated by the scaling in the  $\tilde{Ek} \lesssim 1$  regime, i.e.,  $a_0^* \equiv a_0/[0.15Ra^{0.157}\tilde{Ek}^{-0.05}]$ . Symbols in panels (c) and (d) share the same meaning.

From Figs. 4(a) and 4(c), we can see that the magnitudes of vertical and horizontal velocities are close to each other, which provides a direct experimental support for the assumption of an isotropic velocity in the rapidly rotating limit used in the dimensional analysis in Ref. [26]. We found that the standard deviations of both the horizontal and vertical velocities also show a clear transition at  $\tilde{Ek} \approx 1$  (not shown).

### C. The geometric properties of columnar structures

This section devotes to the geometrical properties of the columnar structures, which are obtained by measuring the horizontal flow fields at height  $z = H/4$ . These structures are first identified by the  $Q$ -criterion method [28], i.e., a connected area  $S$  with  $Q > Q_{th}$  is defined as a single column, as exemplified in Fig. 5(a), which is enlarged to show the identified columns clearly. Here, the threshold value  $Q_{th}$  is chosen to be the standard deviation  $Q_{std}$  of an instantaneous  $Q$  field [29]. Once these structures are identified, an effective radius  $a$  can be calculated as  $a = \sqrt{S/\pi}$  [29]. After averaging over an instantaneous  $Q$  field, its time series  $a(t)$  can be obtained, and some examples for  $Ra = 1.63 \times 10^8$  are displayed in Fig. 5(b). It can be seen that both the mean values  $a_0 = \langle a(t) \rangle_t$  and fluctuations increase with increasing  $Ek$ . This is because the columns undergo complex interactions

[30–33] due to the increased inertial effects at larger  $Ra/Ra_c$  [12]. Next, we focus on the properties of the column's mean radius  $a_0$ .

The slender morphology of the columnar structures suggests a scale separation between the small horizontal and large vertical length scales [9]. Since the formation of these columnar structures is due to the Ekman transport at the Ekman boundary layers, it is more reasonable to normalize the horizontal length scale  $a_0$  by the Ekman boundary layer thickness  $\delta_e = 3HEk^{1/2}$  [27], rather than the large vertical length scale  $H$ . The corresponding results are plotted as a function of  $\widetilde{Ek}$  in Fig. 5(c). It is found that despite the variation in  $Ra$ , all data set, except that of  $Ra = 7.56 \times 10^8$ , show a clear transition at  $\widetilde{Ek} \approx 1$ .

A direct two-dimensional fitting to the data in Fig. 5(c) yields

$$\frac{a_0}{\delta_e} = \begin{cases} 0.15Ra^{0.157 \pm 0.005} \widetilde{Ek}^{-0.05 \pm 0.02}, & \widetilde{Ek} \lesssim 1; \\ 0.06Ra^{0.211 \pm 0.008} \widetilde{Ek}^{-0.43 \pm 0.03}, & \widetilde{Ek} \gtrsim 1. \end{cases} \quad (4)$$

If the scaling in the  $\widetilde{Ek} \gtrsim 1$  regime is rewritten in the form of  $a_0/H$ , the result becomes

$$a_0/H = 0.16Ra^{-0.05 \pm 0.02} Ek^{0.07 \pm 0.03}, \quad \widetilde{Ek} \gtrsim 1. \quad (5)$$

This very weak  $Ek$  dependence is consistent with the experimental results reported by Kunnen *et al.* [29], who found an independence of  $a_0/H$  on  $Ek$  for  $Ra = 6 \times 10^8$  and  $6.7 \times 10^{-6} < Ek < 5.4 \times 10^{-5}$  (i.e.,  $1.5 < \widetilde{Ek} < 12.3$ ). Surprisingly, even the varying range of  $a_0/H$  estimated from Eq. (5) (i.e.,  $0.025 < a_0/H < 0.029$ ) is very close to the measured values from Ref. [29], which fluctuate between 0.022 and 0.026. However, a strong  $Ek$  dependence of  $a_0/H$  was found by Vorobieff *et al.* [34] for  $2.5 < \widetilde{Ek} < 12.3$ . This discrepancy is most likely resulting from the threshold value  $Q_{th} = 0$  adopted in Ref. [34], which would introduce significant errors as pointed out in Ref. [29]. Figure 5(d) shows the compensated plot of  $a_0/\delta_e$ , in which the transition at  $\widetilde{Ek} \approx 1$  becomes more evident.

Flow visualizations of the asymptotic simulation data reveal a decreased column density with increased  $Ra/Ra_c$ , suggesting that the center distance  $d_0$  between two columns may be a relevant characteristic horizontal length scale in the system [11,35]. The calculation of the center distance  $d_0$  is not as straightforward as the radius  $a_0$ . The inspiring work done by Ding *et al.* [36] suggests a good method to estimate the center distance  $d_0$ , which is based on the sharp peaks shown in the Fourier spectra of the vorticity fields. In the present work, the center distance  $d_0$  can be estimated similarly. First, the magnitude of the Fourier transform  $F(\mathbf{k})$  of an instantaneous  $Q$  field was calculated [Fig. 6(a)]. The craterlike structure of  $F(\mathbf{k})$  indicates that the orientation of  $\mathbf{k}$  is irrelevant. Therefore, its dependence is stripped from  $F(\mathbf{k})$  by azimuthal average. The corresponding result  $F(k)$  is displayed in Fig. 6(b), from which a well-defined peak can be identified at the wave number  $k^*$ . We found that as  $Ra/Ra_c$  increases, the peak of  $F(k)$  becomes flatter, but the peak position can still be determined easily. The inset of Fig. 6(b) suggests that this characteristic wave number  $k^*$  captures the size of the craterlike structure reasonably well. With this wave number  $k^*$ , the column's center distance  $d$  can then be defined as  $d = 2\pi/k^*$ . After averaging over time, the mean center distance  $d_0$  can be obtained. Figure 6(c) shows the so-obtained  $d_0$  in our experiments. Similar to the behaviors of  $a_0$  in Fig. 5(c), the normalized center distance  $d_0/\delta_e$  in Fig. 6(c) also depends on  $Ra$  and exhibits a clear transition at  $\widetilde{Ek} \approx 1$ . Again, a direct two-dimensional fitting to the data yields

$$\frac{d_0}{\delta_e} = \begin{cases} 0.32Ra^{0.201 \pm 0.007} \widetilde{Ek}^{0.06 \pm 0.02}, & \widetilde{Ek} \lesssim 1; \\ 0.16Ra^{0.240 \pm 0.003} \widetilde{Ek}^{-0.31 \pm 0.01}, & \widetilde{Ek} \gtrsim 1. \end{cases} \quad (6)$$

If the data in Fig. 6(c) are compensated by the scaling in the  $\widetilde{Ek} \lesssim 1$  regime, the data are well collapsed and the transition at  $\widetilde{Ek} \approx 1$  becomes evident, as shown in Fig. 6(d).

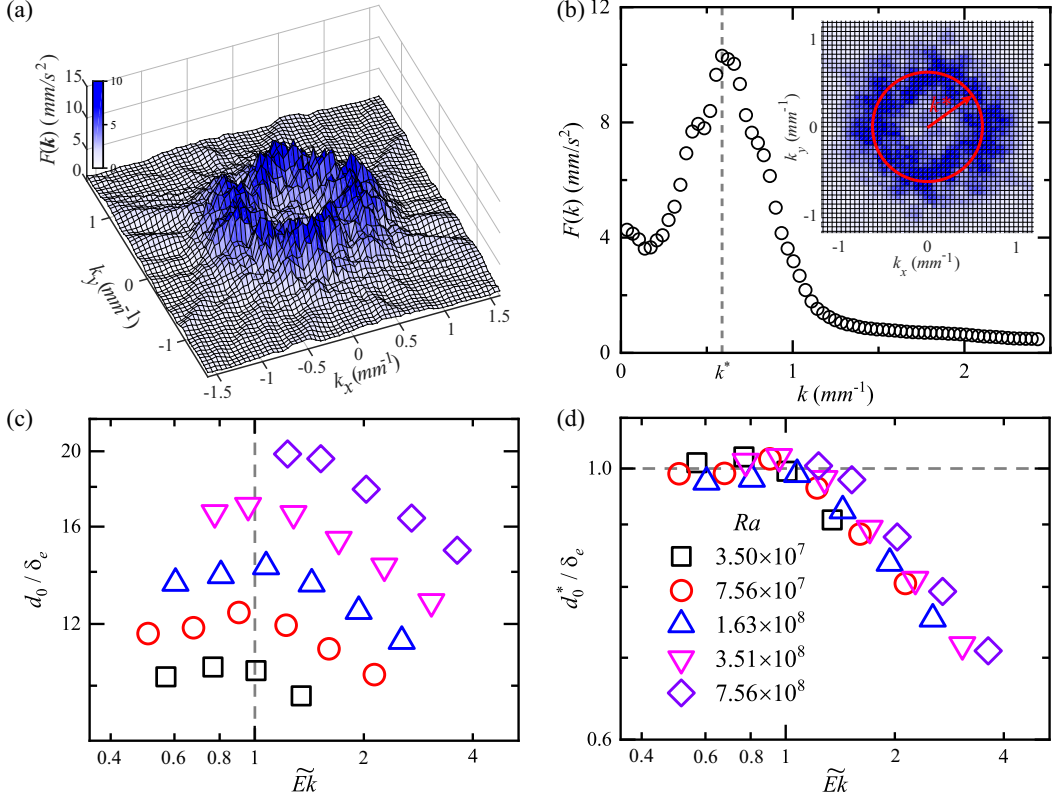


FIG. 6. (a) An example of the magnitude of the Fourier transform  $F(\mathbf{k})$ , showing a craterlike structure. This is calculated from an instantaneous  $Q$  field with  $Ra = 1.63 \times 10^8$  and  $Ek = 7.41 \times 10^{-6}$ . (b) The azimuthally averaged result  $F(k)$  of the spectrum in panel (a), from which the peak at  $k^*$  can be identified easily. The inset is a top view of the spectrum in panel (a), showing that the peak position  $k^*$  captures the size of the craterlike structure correctly. (c) The center distance  $d_0$  normalized by the Ekman boundary layer thickness  $\delta_e$  versus  $\tilde{Ek}$ . (d) The same data as in panel (c) but compensated by the scaling in the  $\tilde{Ek} \lesssim 1$  regime, i.e.,  $d_0^* \equiv d_0 / [0.32Ra^{0.201}\tilde{Ek}^{0.06}]$ . Symbols in panels (c) and (d) share the same meaning.

#### D. $a_0$ and $d_0$ normalized by the critical onset wavelength $L_c$

In Fig. 5 and Fig. 6, the horizontal length scales  $a_0$  and  $d_0$  are normalized by the Ekman boundary layer thickness  $\delta_e$  to show sharp transitions at  $Ek = Ek_t$ . In RRBC, the critical wavelength  $L_c = 4.8Ek^{1/3}$  [37] at onset Rayleigh is an important and extensively-used small horizontal length scale (e.g., Refs. [10,16]). It is also relevant when the viscous force dominates over other forces to balance the Coriolis force [38]. Therefore, in Figs. 7(a) and 7(c), the critical wavelength  $L_c$  is used to normalized  $a_0$  and  $d_0$ . It can be seen that the transitions at  $\tilde{Ek} \approx 1$  can also be observed. A direct two-dimensional fitting to these data in Figs. 7(a) and 7(c) yields, respectively,

$$\frac{a_0}{L_c} = \begin{cases} 0.091Ra^{0.056 \pm 0.005}\tilde{Ek}^{0.12 \pm 0.02}, & \tilde{Ek} \lesssim 1; \\ 0.036Ra^{0.110 \pm 0.009}\tilde{Ek}^{-0.27 \pm 0.03}, & \tilde{Ek} \gtrsim 1, \end{cases} \quad (7)$$

and

$$\frac{d_0}{L_c} = \begin{cases} 0.20Ra^{0.100 \pm 0.006}\tilde{Ek}^{0.23 \pm 0.02}, & \tilde{Ek} \lesssim 1; \\ 0.10Ra^{0.139 \pm 0.004}\tilde{Ek}^{-0.14 \pm 0.01}, & \tilde{Ek} \gtrsim 1. \end{cases} \quad (8)$$

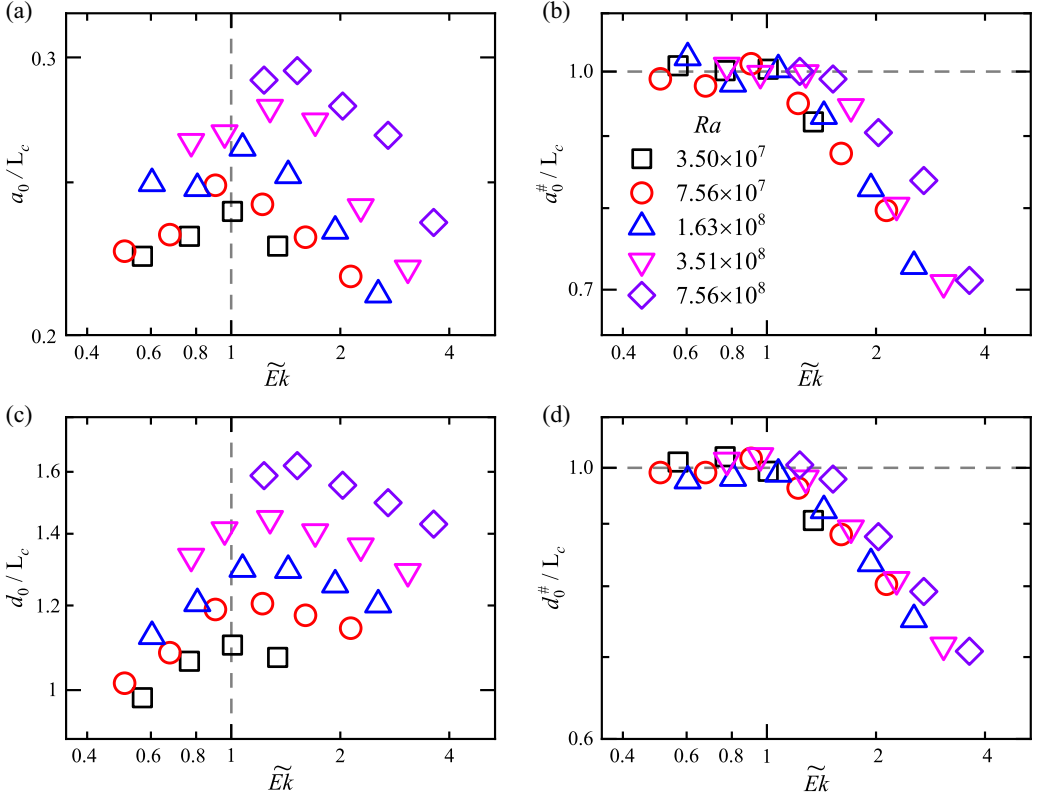


FIG. 7. (a) The mean radius of columnar structures  $a_0$  normalized by the critical onset wavelength  $L_c$  versus  $\widetilde{Ek}$ . (b) The same data as in panel (a) but compensated by the scaling in the  $\widetilde{Ek} \lesssim 1$  regime, i.e.,  $a_0^\# \equiv a_0 / [0.091 Ra^{0.056} \widetilde{Ek}^{0.12}]$ . Similar plots for the center distance  $d_0$  are shown in panels (c) and (d), with  $d_0^\# \equiv d_0 / [0.2 Ra^{0.1} \widetilde{Ek}^{0.23}]$ .

If these results are compensated by the scaling in the  $\widetilde{Ek} \lesssim 1$  regime, the transitions at  $\widetilde{Ek} \approx 1$  become more evident, as shown in Figs. 7(b) and 7(d). In this regard, the length scale  $L_c$  is also a good choice.

It can be seen that both  $a_0$  and  $d_0$  do not exhibit the one-third scaling on  $Ek$ . Song *et al.* [39] have shown that this scaling can be only observed very close to  $Ra_c$  with  $Ra/Ra_c < 2$ . In the present study, there is not enough data in this limited parameter range to reveal the one-third scaling [refer to Fig. 1(d)].

The scale separation between small horizontal and large vertical length scales is an important basis for the asymptotically-reduced model [10,40] and the dimensional analysis [26] in RRBC. The vertical scale is straightforward; it is the cell's height  $H$ . The horizontal scale has been investigated using the mean kinetic energy spectrum [38] or the correlation functions [16]. However, neither provides a clear physical meaning for the introduced small horizontal scales. In the present study, two different kinds of horizontal length scales are determined experimentally with clear physical meanings, which will be essential in the quantitative study of the morphology and dynamics of the coherent structures. For instance, one should concern about the column's size (i.e., the radius  $a_0$ ) when investigating the properties of CTCs [9,41,42]. As for the column's horizontal dynamics, the separation between nearby columns (i.e., the center distance  $d_0$ ) is more relevant, since it would undoubtedly affect the column's interacting frequency and strength [43].

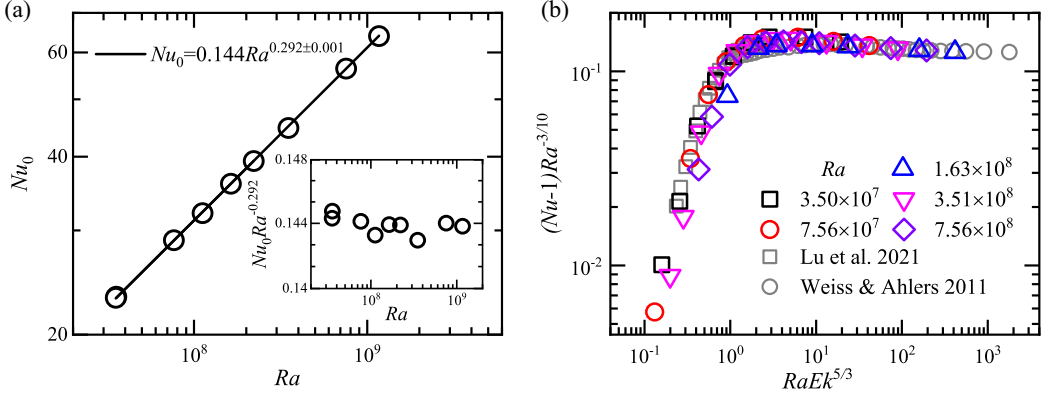


FIG. 8. (a) The heat-transfer scaling without rotation. Inset: compensated plot. (b) The heat-transport data are plotted as suggested by the theoretical model proposed in Ref. [7]. The data with gray open squares are from Ref. [20] with  $Ek = 7.4 \times 10^{-6}$  and various  $Ra$ , and the data with gray open circles are from Ref. [52] with  $Ra = 2.3 \times 10^9$  and various  $Ek$ .

#### IV. CONCLUSIONS AND IMPLICATIONS

In summary, we have conducted an experimental study of the heat transport and properties of the dynamics and geometric structures of the flow field in rotating Rayleigh-Bénard convection, and find experimentally that both heat transport and flow structures exhibit a clear transition at a transitional Ekman number  $Ek_t$ . This correspondence reveals that (i) the behaviors of heat-transfer efficiency are intimately related to the changes of coherent structures in the bulk flow in terms of flow dynamics and morphology; (ii) the clear transition at  $Ek_t$  is the first unequivocal experimental evidence for the regime transition from CTC to plume regimes, at which the columns break down as a result of the increased inertial effect; (iii) compared to the  $Nu$  behaviors, the transitions of the flow dynamics and morphology are much sharper, which suggests that flow-field measurements may be used as a more convincing criterion for regime transitions.

The present findings may have some implications for the planetary dynamos, especially for the geodynamo studies. The planets in our solar system exhibit different magnetic-field topologies [44]. The dipolar fields observed in most solar planets are thought to be created by columnar structures in the convective cores [45], whereas the mysterious multipolar fields in Uranus and Neptune are very likely caused by the more turbulent flows with strong inertial effects [44], which are also revealed by numerical dynamo models (e.g., Refs. [46–48]). Therefore, the identification of the dipole-multipole transition is of particular interest. What's more interesting as found in numerical models is that occasional dipole reversals occur near the dipole-multipole transition [49], which resembles the recorded behaviors of Earth's magnetism [50]. This resemblance implies that the flow state of the Earth's core should lie within the dipolar regime but close to the dipole-multipole transition [49], i.e., the Rayleigh number for the Earth's core  $Ra_E$  should be a little bit smaller than the transitional  $Ra_t$  for the column to plume regime transition. From the boundary-layer crossing mechanism [51] and the intersection of steep  $Nu - Ra$  scaling with nonrotating results [19], different transitional Rayleigh numbers  $Ra_t = Ek^{-7/4}$  and  $Ra_t = 5.4Ek^{-1.466}$  are derived, respectively. With the values  $Ra_E = 2 \times 10^{24}$  and  $Ek_E = 1.3 \times 10^{-15}$  estimated for the Earth's core [51],  $Ra_E/Ra_t$  are estimated to be 0.02 and 55.6, respectively, for the above two methods. Both are far from unity. In contrast, the present result  $Ra_t = 0.71Ek^{-1.66}$  [Eq. (1)] provides a better estimation  $Ra_E/Ra_t \approx 0.6$  for geodynamo, namely, it is in the dipolar regime but near the dipole-multipole transition.

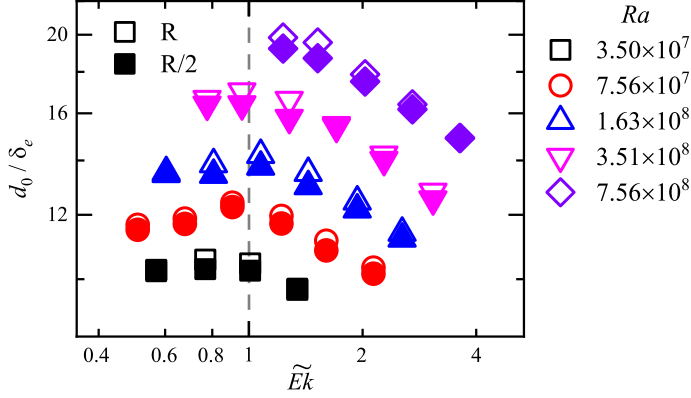


FIG. 9. A comparison between the results of  $d_0$  obtained from the flow fields covering different areas  $\pi r^2$  with  $r = R$  (open symbols) and  $r = R/2$  (solid symbols).

### ACKNOWLEDGMENTS

This work is supported by the National Natural Science Foundation of China (NSFC) (Grants No. 12072144 and No. 12232010). L.Q.W. acknowledges financial support by the Research Grants Council of Hong Kong (Grants No. 17205421, No. 17204420, and No. 17213823).

### APPENDIX A: COMPARISON WITH THE THEORETICAL MODEL OF HEAT TRANSPORT

In this section, the measured Nu data are replotted to verify the theoretical model proposed by Ecke and Shishkina [7]. In this model, the steep scaling  $\text{Nu} \sim (\text{Ra}/\text{Ra}_c)^\gamma$  in the rotation-dominated regime is related to the nonrotating scaling  $\text{Nu} \sim \text{Ra}^{\gamma_0}$  via the assumption of crossing between Ekman and thermal boundary layers, based on which a relation  $\gamma_0 = 3\gamma/(3 + 8\gamma)$  can be derived. With  $\gamma = 1.5$  obtained in current study, the predicted value of  $\gamma_0$  is  $3/10$ , which agrees well with the measured result  $\gamma_0 = 0.292$  [Fig. 8(a)].

Ecke and Shishkina [7] further proposed that one can collapse the data by plotting  $(\text{Nu} - 1)/\text{Ra}^{\gamma_0}$  versus  $\text{Ek}^{1/(2\gamma_0)}\text{Ra}$ . Therefore, in Fig. 8(b), the rescaled Nusselt number  $(\text{Nu} - 1)\text{Ra}^{-3/10}$  is plotted as a function of  $\text{Ra}\text{Ek}^{5/3}$ . The experimental results from Ref. [20] (gray open squares) and Ref. [52] (gray open circles) are also displayed as a comparison. The collapsed behaviors of present data and previous results show a nice consistency with the proposed model in Ref. [7].

### APPENDIX B: NEGLIGIBLE EFFECTS OF WEAK CENTRIFUGAL FORCE ON $a_0$ AND $d_0$

The Froude number range of present study is in the weak-centrifugal regime with  $\text{Fr}_c < \text{Fr} < \Gamma/2$ . Here, we demonstrate that the properties of columnar structures (e.g.,  $a_0$  and  $d_0$ ) are not affected by the weak centrifugal force.

At very large centrifugal force, slender columnar structures are replaced by a large hot coherent structure at cell center [23]. However, the centrifugal force here is not strong enough and individual columns can still be recognized [as shown in Figs. 2(a)–2(c)]. Since the column's radius  $a_0$  are calculated from these individual columns, it can be expected that its results are not affected by the weak centrifugal force.

To reveal the possible influence of centrifugal force on the center distance  $d_0$ , the results obtained from the flow fields covering different areas  $\pi r^2$  with  $r = R/2$  and  $R$ , are compared in Fig. 9. It can be seen that the results are almost the same, and thus we can safely conclude that the effect of the weak centrifugal force on  $d_0$  is negligible.

- [1] A. Adriani, A. Mura, G. Orton, C. Hansen, F. Altieri, M. L. Moriconi, J. Rogers, G. Eichstädt, T. Momary, A. P. Ingersoll, G. Filacchione, G. Sindoni, F. Tabataba-Vakili, B. M. Dinelli, F. Fabiano, S. J. Bolton, J. E. P. Connerney, S. K. Atreya, J. I. Lunine, F. Tosi, A. Migliorini, D. Grassi, G. Piccioni, R. Noschese, A. Cicchetti, C. Plainaki, A. Olivieri, M. E. O’Neill, D. Turrini, S. Stefani, R. Sordini, and M. Amoroso, Clusters of cyclones encircling Jupiter’s poles, *Nature (London)* **555**, 216 (2018).
- [2] D. W. Waugh, Fluid dynamics of polar vortices on earth, mars, and titan, *Annu. Rev. Fluid Mech.* **55**, 265 (2023).
- [3] S. V. Berdyugina, Starspots: A key to the stellar dynamo, *Living Rev. Solar Phys.* **2**, 8 (2005).
- [4] A. Provenzale, Transport by coherent barotropic vortices, *Annu. Rev. Fluid Mech.* **31**, 55 (1999).
- [5] R. J. A. M. Stevens, H. J. H. Clercx, and D. Lohse, Heat transport and flow structure in rotating Rayleigh–Bénard convection, *Eur. J. Mech. B Fluids* **40**, 41 (2013).
- [6] R. P. J. Kunnen, The geostrophic regime of rapidly rotating turbulent convection, *J. Turbul.* **22**, 267 (2021).
- [7] R. E. Ecke and O. Shishkina, Turbulent rotating Rayleigh–Bénard convection, *Annu. Rev. Fluid Mech.* **55**, 603 (2023).
- [8] T. Gastine and J. M. Aurnou, Latitudinal regionalization of rotating spherical shell convection, *J. Fluid Mech.* **954**, R1 (2023).
- [9] I. Grooms, K. Julien, J. B. Weiss, and E. Knobloch, Model of convective Taylor columns in rotating Rayleigh–Bénard convection, *Phys. Rev. Lett.* **104**, 224501 (2010).
- [10] M. Sprague, K. Julien, E. Knobloch, and J. Werne, Numerical simulation of an asymptotically reduced system for rotationally constrained convection, *J. Fluid Mech.* **551**, 141 (2006).
- [11] K. Julien, A. M. Rubio, I. Grooms, and E. Knobloch, Statistical and physical balances in low Rossby number Rayleigh–Bénard convection, *Geophys. Astrophys. Fluid Dyn.* **106**, 392 (2012).
- [12] A. J. Aguirre Guzmán, M. Madonia, J. S. Cheng, R. Ostilla-Mónico, H. J. H. Clercx, and R. P. J. Kunnen, Force balance in rapidly rotating Rayleigh–Bénard convection, *J. Fluid Mech.* **928**, A16 (2021).
- [13] K. Julien, E. Knobloch, A. M. Rubio, and G. M. Vasil, Heat transport in low-Rossby-number Rayleigh–Bénard convection, *Phys. Rev. Lett.* **109**, 254503 (2012).
- [14] J. S. Cheng, J. M. Aurnou, K. Julien, and R. P. J. Kunnen, A heuristic framework for next-generation models of geostrophic convective turbulence, *Geophys. Astrophys. Fluid Dyn.* **112**, 277 (2018).
- [15] J. S. Cheng, M. Madonia, A. J. Aguirre Guzmán, and R. P. J. Kunnen, Laboratory exploration of heat transfer regimes in rapidly rotating turbulent convection, *Phys. Rev. Fluids* **5**, 113501 (2020).
- [16] D. Nieves, A. M. Rubio, and K. Julien, Statistical classification of flow morphology in rapidly rotating Rayleigh–Bénard convection, *Phys. Fluids* **26**, 086602 (2014).
- [17] H. Rajaei, R. P. J. Kunnen, and H. J. H. Clercx, Exploring the geostrophic regime of rapidly rotating convection with experiments, *Phys. Fluids* **29**, 045105 (2017).
- [18] M. Madonia, A. J. Aguirre Guzmán, H. J. H. Clercx, and R. P. J. Kunnen, Velocimetry in rapidly rotating convection: Spatial correlations, flow structures and length scales, *Europhys. Lett.* **135**, 54002 (2021).
- [19] J. S. Cheng, S. Stellmach, A. Ribeiro, A. Grannan, E. M. King, and J. M. Aurnou, Laboratory-numerical models of rapidly rotating convection in planetary cores, *Geophys. J. Int.* **201**, 1 (2015).
- [20] H.-Y. Lu, G.-Y. Ding, J.-Q. Shi, K.-Q. Xia, and J.-Q. Zhong, Heat-transport scaling and transition in geostrophic rotating convection with varying aspect ratio, *Phys. Rev. Fluids* **6**, L071501 (2021).
- [21] Y.-B. Hu, Y.-C. Xie, and K.-Q. Xia, On the centrifugal effect in turbulent rotating thermal convection: onset and heat transport, *J. Fluid Mech.* **938**, R1 (2022).
- [22] P. P. Niiler and F. E. Bisshopp, On the influence of coriolis force on onset of thermal convection, *J. Fluid Mech.* **22**, 753 (1965).
- [23] S. Horn and J. M. Aurnou, Regimes of Coriolis-centrifugal convection, *Phys. Rev. Lett.* **120**, 204502 (2018).
- [24] The steep  $Nu - Ra$  scaling at small  $Ra/Ra_c$  conforms to the shallow scaling at large  $Ra/Ra_c$  through a transitional regime. The upper bound of the steep scaling regime determined by the ‘extrapolation’ method proposed in [19] reaches into the transitional regime a little bit, that is, overestimates the upper bound a

- little bit (see Figure 7 in [19]). In this regard, the result obtained by intersecting two locally fitted power laws [20] is closer to the ‘real’ upper bound (see Figure 3 in [20]).
- [25] E. K. Hawkins, J. S. Cheng, J. A. Abbate, T. Pilegard, S. Stellmach, K. Julien, and J. M. Aurnou, Laboratory models of planetary core-style convective turbulence, [Fluids](#) **8**, 106 (2023).
  - [26] J. M. Aurnou, S. Horn, and K. Julien, Connections between nonrotating, slowly rotating, and rapidly rotating turbulent convection transport scalings, [Phys. Rev. Res.](#) **2**, 043115 (2020).
  - [27] E. M. King, S. Stellmach, and J. M. Aurnou, Heat transfer by rapidly rotating Rayleigh–Bénard convection, [J. Fluid Mech.](#) **691**, 568 (2012).
  - [28] J. C. R. Hunt, A. A. Wray, and P. Moin, Eddies, streams, and convergence zones in turbulent flows, in *Center for Turbulence Research Report CTR-S88* (Stanford University, Stanford, 1988), pp. 193–208.
  - [29] R. P. J. Kunnen, H. J. H. Clercx, and B. J. Geurts, Vortex statistics in turbulent rotating convection, [Phys. Rev. E](#) **82**, 036306 (2010).
  - [30] B. M. Boubnov and G. S. Golitsyn, Experimental study of convective structures in rotating fluids, [J. Fluid Mech.](#) **167**, 503 (1986).
  - [31] F. Zhong, R. E. Ecke, and V. Steinberg, Rotating Rayleigh–Bénard convection: asymmetric modes and vortex states, [J. Fluid Mech.](#) **249**, 135 (1993).
  - [32] K. Julien, S. Legg, J. McWilliams, and J. Werne, Rapidly rotating turbulent Rayleigh–Bénard convection, [J. Fluid Mech.](#) **322**, 243 (1996).
  - [33] D. Noto, Y. Tasaka, T. Yanagisawa, and Y. Murai, Horizontal diffusive motion of columnar vortices in rotating Rayleigh–Bénard convection, [J. Fluid Mech.](#) **871**, 401 (2019).
  - [34] P. Vorobieff and R. E. Ecke, Vortex structure in rotating Rayleigh–Bénard convection, [Physica D](#) **123**, 153 (1998).
  - [35] This new horizontal length scale mentioned in [11] is the inter-column distance. In this paper, the center-distance and the inter-column distance are equivalent to some extent, *i.e.* both reflect the separation between nearby columns. If we take the finite size of these columnar structures into consideration, their inter-column distance can be simply estimated as  $d_0 - 2a_0$ .
  - [36] S.-S. Ding, H.-L. Zhang, D.-T. Chen, and J.-Q. Zhong, Vortex patterns in rapidly rotating Rayleigh–Bénard convection under spatial periodic forcing, [J. Fluid Mech.](#) **950**, R1 (2022).
  - [37] S. Chandrasekhar, *Hydrodynamic and Hydromagnetic Stability* (Oxford University Press, Oxford, 1961).
  - [38] E. M. King, S. Stellmach, and B. Buffett, Scaling behaviour in Rayleigh–Bénard convection with and without rotation, [J. Fluid Mech.](#) **717**, 449 (2013).
  - [39] J. Song, O. Shishkina, and X. Zhu, Direct numerical simulations of rapidly rotating Rayleigh–Bénard convection with Rayleigh number up to  $5 \times 10^{13}$ , [J. Fluid Mech.](#) **989**, A3 (2024).
  - [40] K. Julien, E. Knobloch, and J. Werne, A new class of equations for rotationally constrained flows, [Theor. Comput. Fluid Dyn.](#) **11**, 251 (1998).
  - [41] J. W. Portegies, R. P. J. Kunnen, G. J. F. van Heijst, and J. Molenaar, A model for vortical plumes in rotating convection, [Phys. Fluids](#) **20**, 066602 (2008).
  - [42] J.-Q. Shi, H.-Y. Lu, S.-S. Ding, and J.-Q. Zhong, Fine vortex structure and flow transition to the geostrophic regime in rotating Rayleigh–Bénard convection, [Phys. Rev. Fluids](#) **5**, 011501(R) (2020).
  - [43] K. L. Chong, J.-Q. Shi, G.-Y. Ding, S.-S. Ding, H.-Y. Lu, J.-Q. Zhong, and K.-Q. Xia, Vortices as Brownian particles in turbulent flows, [Sci. Adv.](#) **6**, eaaz1110 (2020).
  - [44] G. Schubert and K. M. Soderlund, Planetary magnetic fields: Observations and models, [Phys. Earth Planet. Inter.](#) **187**, 92 (2011).
  - [45] C. A. Jones, Planetary magnetic fields and fluid dynamos, [Annu. Rev. Fluid Mech.](#) **43**, 583 (2011).
  - [46] C. Kutzner and U. R. Christensen, From stable dipolar towards reversing numerical dynamos, [Phys. Earth Planet. Inter.](#) **131**, 29 (2002).
  - [47] B. Sreenivasan and C. A. Jones, The role of inertia in the evolution of spherical dynamos, [Geophys. J. Int.](#) **164**, 467 (2006).
  - [48] L. Oruba and E. Dormy, Transition between viscous dipolar and inertial multipolar dynamos, [Geophys. Res. Lett.](#) **41**, 7115 (2014).

- [49] P. Olson and U. R. Christensen, Dipole moment scaling for convection-driven planetary dynamos, [Earth Planet. Sci. Lett. \*\*250\*\*, 561 \(2006\)](#).
- [50] P. H. Roberts and E. M. King, On the genesis of the Earth's magnetism, [Rep. Prog. Phys. \*\*76\*\*, 096801 \(2013\)](#).
- [51] E. M. King, K. M. Soderlund, U. R. Christensen, J. Wicht, and J. M. Aurnou, Convective heat transfer in planetary dynamo models, [Geochem. Geophys. Geosyst. \*\*11\*\*, 2010GC003053 \(2010\)](#).
- [52] S. Weiss and G. Ahlers, The large-scale flow structure in turbulent rotating Rayleigh-Bénard convection, [J. Fluid Mech. \*\*688\*\*, 461 \(2011\)](#).